Interstitial Oxide Ion Distribution and Transport Mechanism in Aluminum-doped Neodymium Silicate Apatite Electrolytes

An, Tao; Baikie, Tom; Orera, Alodia; Piltz, Ross; Meven, Martin; Slater, Peter; Wei, Jun; Sanjuan, Maria; White, Timothy

DOI:
10.1021/jacs.5b13409

Interstitial Oxide Ion Distribution and Transport Mechanism in Aluminum-doped Neodymium Silicate Apatite Electrolytes

Tao An,[†] Tom Baikie,[‡] Alodia Orera,[∥] Ross O. Piltz,[§] Martin Meven,[⊥] Peter R. Slater,[¶] Jun Wei,*[,#] María L. Sanjuán,[∥] and Tim J. White*[,†]

[†]*Nanyang Technological University, School of Materials Science and Engineering, 50 Nanyang Avenue, Singapore 639798, Singapore,* [‡]*Energy Research Institute @ NTU (ERI@N), Nanyang Technological University, Singapore 637553, Singapore*, [∥]ICMA, CSIC-Universidad de Zaragoza, 50009 Zaragoza, Spain, [§]*Bragg Institute, Australian Science and Technology Organisation, Lucas Heights, NSW 2234, Australia*, [⊥]FZ Jülich GmbH, Jülich Centre for Neutron Science (JCNS) at FRM II, Lichtenbergstraße 1, D-85727 Garching, Germany, [¶]School of Chemistry, University of Birmingham, Edgbaston, Birmingham, B15 2TT, UK, and [#]*Singapore Institute of Manufacturing Technology (SIMTech), Agency for Science, Technology and Research (A*STAR), 71 Nanyang Drive, 638075, Singapore.*

KEYWORDS : solid electrolyte, apatite, crystal structure, neutron diffraction, oxygen interstitial, conduction path

ABSTRACT: Rare earth silicate apatites are one-dimensional channel structures that show potential as electrolytes for solid oxide fuel cells (SOFC) due to their high ionic conductivity at intermediate temperatures (500 – 700°C). This advantageous property can be attributed to the presence of both interstitial oxygen and cation vacancies, that create diffusion paths which computational studies suggest are less tortuous and have lower activation energies for migration than in stoichiometric compounds. In this work, neutron diffraction of $Nd_{(28+x)/3}Al_xSi_{6-x}O_{26}$ ($0 \le x \le 1.5$) single crystals identified the locations of oxygen interstitials, and allowed the deduction of a dual-path conduction mechanism that is a natural extension of the single-path sinusoidal channel trajectory arrived at through computation. This discovery provides the most thorough understanding of the O^{2-} transport mechanism along the channel to date, clarifies the mode of inter-channel motion, and presents a complete picture of O^{2-} percolation through apatite. Previously reported crystallographic and conductivity measurements are re-examined in the light of these new findings.

■ INTRODUCTION

The solid oxide fuel cell (SOFC) is a device that generates electricity from the chemical energy of oxidizable fuels without combustion, leading to much lower and non-polluting gaseous emissions than conventional hydrocarbon-based power production.[1] Compared to other types of high temperature fuel cells, such as the molten carbonate fuel cell (MCFC), the elimination of a liquid phase in the SOFC leads to higher efficiency, greater chemical and physical stability, and provides flexibility in the choice of fuel.[2] Typically, this technology operates at elevated temperatures, which promotes seal failures, necessitates long start-up times, and requires expensive interconnect materials.[3] Ionic conduction in the baseline solid electrolyte, yttria-stabilized zirconia (YSZ), is by vacancy transport and significant above 1000°C.[4] Therefore, the need exists to discover alternative solid electrolytes that function from 500 to 700°C. To this end, lanthanoid (*Ln*) silicate/germanate ($Ln_{9.33}(Si/Ge)_6O_{26}$) apatite tunnel structures, through which oxygen can readily migrate, are being examined as intermediate temperature electrolytes.[5]

The structural formula of $Ln_{9.33}Si_6O_{26}$ with $P6_3/m$ symmetry can be expressed as $[Ln^F_{3.33}\square_{0.67}][Ln^T_6][(SiO_4)_6][O_2]$.[6] In terms of descriptive crystallography, rigid SiO_4 tetrahedra are corner-connected to Ln^FO_6 metaprisms that form a framework surrounding the Ln^T atoms, which in turn enclose the tunnel oxygens (Figure 1).[7] To satisfy charge balance, this compound is cation-deficient with the *Ln* vacancies located at the framework site.[8] It has been suggested that these cation vacancies create space for interstitial oxygen,[9] enabling alternative O^{2-} transport paths with lower activation energies.[10] Thus, electrolyte performance is controlled by the cation vacancy and O^{2-} interstitial concentration. For example, in $La_{9.33+x/3}\square_{0.67-x/3}Al_xSi_{6-x}O_{26}$ ($0 \le x \le 2$) apatite, the chemical tailoring of Al content ($\square_{La} + 3Si^{4+} \rightarrow La^{3+} + 3Al^{3+}$ most simply) balances steric enhancement due to larger Al expanding the conducting channel against vacancy removal that blocks

conduction. Consequently, the highest O^{2-} transport is achieved at the compromise composition x = 1.5, while fully stoichiometric $La_{10}Al_2Si_4O_{26}$ (x = 2) has the lowest conductivity as interstitial transport is denied by the elimination of cation vacancies.[11] As a further example, the oxygen-excess series $La_{9.33+2x/3}Si_6O_{26+x}$ (0 ≤ x ≤ 0.5) has higher conductivity due to extra-stoichiometric interstitial O^{2-}, with maximum mobility achieved for $La_{9.67}Si_6O_{26.5}$ (x = 0.5), as La_2SiO_5 appears as a secondary phase for x > 0.5 which detracts from overall performance.[12] However, most studies use polycrystalline samples, due to the rarity of large single crystals, and the analysis of intrinsic mobility requires deconvolution from the grain boundary component. Moreover, despite frequent references to "$La_{10}Si_6O_{27}$",[13] the existence of this compound is dubious as steric restrictions lead to significant M-O (M = La, Si) overbonding. This is in contrast to $La_{10}Ge_6O_{27}$, where lattice expansion (IR_{Ge} > IR_{Si}) allows complete filling of interstitial positions.[14]

For $P6_3/m$ lanthanoid silicate apatites, both first principles simulation[15-17] and neutron diffraction[18] found O^{2-} interstitial migration follows a sinusoidal transport route along the c-axis,[9] passing through saddle points near the SiO_4 tetrahedra at the channel periphery to create pseudo-SiO_5 units, or involves in the co-operative displacement with tunnel oxygen.[16,17] Simultaneously, conduction of O^{2-} across the *ab* basal plane is enabled by the presence of interstitials near to, or within, the *Ln* vacant sites in both silicate[17] and germanate[14] apatites; but such mobility is less significant due to the higher activation energy required.[19,20] Modelling and ^{17}O NMR work has also suggested the importance of exchange processes involving the Si/GeO_4 in this respect.

In our recent study, large single crystals of Al-doped neodymium silicate apatite, $Nd_{(28+x)/3}Al_xSi_{6-x}O_{26}$ (0 ≤ x ≤ 1.5) were successfully grown.[21] The high quality of the material was confirmed by powder X-ray diffraction, electron backscatter diffraction and energy dispersive X-ray spectroscopy, with structural features matched to O^{2-} mobility assessed by AC impedance spectroscopy.[22] The undoped $Nd_{9.33}Si_6O_{26}$ was well described in $P6_3/m$,[23] but the Al-doped crystals showed poorer goodness-of-fit (GOF) due to Nd and O(3) site disorder. Undoped $Nd_{9.33}Si_6O_{26}$ displayed strong anisotropic ionic conductivity, and while the temperature dependent conductivity plot is linear across the *ab* basal plane, a clear inflection appears in the c axis conductivity at ~500°C. This feature disappeared upon annealing at 950°C for 3 months and the overall conductivity was lowered. Al-doping increased the conductivity across the *ab* plane, but mobility was degraded in the c axis direction, to yield an overall improvement for polycrystalline samples.[24]

In this work, neutron diffraction was performed to validate and extend the X-ray study of $Nd_{(28+x)/3}Al_xSi_{6-x}O_{26}$ single crystals with a particular emphasis on recognizing split oxygen positions and discovering low concentration interstitial oxygen. With the aim of throwing light into the interplay between cation vacancies, oxygen interstitial or split sites and other structural aspects such as long-range symmetry of these apatites, we have measured the Raman spectrum of $Nd_{9.33}Si_6O_{26}$ single crystals (both as-grown and annealed) and compared to that of $Nd_8Sr_2Si_6O_{26}$,[25] which serves as reference material due to absence of vacancies and oxygen split sites, and negligible or very low O_{int} content. The availability of single crystals allows the correct interpretation of the spectra, as it puts into evidence modes with close or even identical frequencies but with different symmetries that would be indistinguishable in polycrystalline specimens. Ion mobility was inspected over a range of temperatures for the undoped crystal, and the effect of crystallochemical incorporation of aluminum on interstitial abundance and location was correlated with conductivity measurements. From these findings, the conduction paths both along the c axis and across the *ab* plane were deduced and compared with published simulation mechanisms.

■ EXPERIMENTAL METHODS

Single crystals of $Nd_{(28+x)/3}Al_xSi_{6-x}O_{26}$ (0 ≤ x ≤ 1.5) were grown by the floating zone method as described elsewhere.[21] Preliminary structures were extracted from X-ray diffraction and ionic conductivities measured along the c axis and across the *ab* plane.[22] Raman measurements were carried out and analyzed in a similar manner as the previous study on $Nd_8Sr_2Si_6O_{26}$ single crystals, which was described in details elsewhere.[25] Single crystal neutron diffraction was carried out with both the white beam radiation Laue method and a fixed wavelength four-circle method.

Laue method. Single crystal neutron diffraction data were collected on the KOALA Laue diffractometer at the Open Pool Australian Lightwater (OPAL) reactor operated by the Australian Nuclear Science and Technology Organisation (ANSTO). The Laue method uses polychromatic thermal-neutrons coupled with a large solid-angle (8 steradians) cylindrical image-plate detector. The as-grown apatite crystals of approximate dimensions 1.5 × 1.5 × 1.5 mm were mounted on an aluminum pin with silicone grease. The diffraction patterns were indexed using LAUEGEN[26,27] and the reflections integrated using a 2D version of the $\sigma(I)/I$ algorithm described by Wilkinson *et al.*[28] and Prince *et al.*[29]. No absorption correction was necessary. The reflections were normalized to the same incident wavelength using a curve derived by comparing equivalent reflections and multiple observations via the program LAUENORM.[30] Only reflections with wavelengths between 1.0 Å and 2.9 Å were accepted as those outside this range were too weak, or had too few equivalents, to allow determination of the normalization curve confidently. Structures were determined using Jana 2006[31] with the starting model derived from single crystal X-ray diffraction.[22] VESTA[32] was used for 3D visualization of the difference Fourier maps that allow identification of structural disorder and interstitial oxygen. Data were collected at 4, 100, 300, 573 and 773K for the undoped $Nd_{9.33}Si_6O_{26}$ crystal. For the x = 0.5, 1.0 and 1.5 Al-doped $Nd_{(28+x)/3}Al_xSi_{6-x}O_{26}$ data were accumulated at 100K.

Fixed wavelength four-circle method. To validate outcomes from the Laue experiments, single crystal neu-

tron diffraction data were also collected from as-grown $Nd_{9.33}Si_6O_{26}$ crystals at 2K and room temperature, and for an annealed $Nd_{9.33}Si_6O_{26}$ crystal (950°C/3 months) at room temperature on the HEiDi diffractometer at FRM-II (Heißes Einkristalldiffraktometer, hot source, Garching, Germany). A wavelength of 1.17Å combined with a high flux density of 1.4×10^7 neutrons per second per cm^2 was obtained using an Er filter and a Ge (311) monochromator. Low temperatures were realised by a He closed-cycle cryostat mounted in the Eulerian cradle of the diffractometer. The crystal was wrapped in Al foil to minimize thermal loses and the temperature measured and controlled by a diode sensor near the heater to a stability of ± 0.1K. The absolute temperatures were measured by an additional temperature sensor at the sample. The corrected integrated intensities of the reflections were calculated using PRON2K,[33] and numerical absorption correction was performed with TBAR.[34] Further instrument details can be found in Hutanu *et al*.[35]

■ RESULTS

In previous work of single crystal X-ray diffraction, O(3)' split sites were identified only in undoped as-grown $Nd_{9.33}Si_6O_{26}$ single crystals.[22] Such features, however, were found in both Al-doped $Nd_{(28+x)/3}Al_xSi_{6-x}O_{26}$ (x = 0.5, 1.0 and 1.5) and annealed $Nd_{9.33}Si_6O_{26}$ single crystals in this neutron study. This is mainly due to the fact that a much larger volume was inspected during the neutron diffraction experiment, and neutrons are more sensitive to oxygen positions, while the single crystal X-ray diffraction data were dominated by the contribution from the heavier Nd element. While the space group for $Nd_{9.33}Si_6O_{26}$ apatite is reportedly $P6_3/m$, based on single crystal X-ray diffraction data,[23] a careful neutron diffraction study on $La_{9.33}Si_6O_{26}$ suggested the true symmetry of this La analogue to be $P6_3$.[36] Therefore, both $P6_3/m$ and $P6_3$ models were tested for the fixed wavelength diffraction data collected at 2K. In $P6_3$, removal of the mirror plane perpendicular to c axis allows the framework 4*f* Nd(1) site to split into two 2*b* sites, Nd(1) and Nd(2), and the 12*i* O(3) splits into two 6c sites, O(3) and O(4) (Table 1). Introducing this extra degree of freedom at the former site enables better fitting of the cation vacancies by ensuring no Nd vacancies can occur next to each other, and a slightly improved GOF compared to $P6_3/m$ (Table 2), which, however, did not fundamentally improve the quality of the structure determination.

To confirm the space group of $Nd_{9.33}Si_6O_{26}$ as well as the oxygen site splitting, Raman spectroscopy was carried out on the single crystal samples. The expected Raman activity for $P6_3$ and $P6_3/m$ space group is shown in Tables S1 and S2 (Supplementary Information), respectively. The higher activity in $P6_3$ comes from the loss of inversion symmetry in this space group. It should be noted that the total number of expected modes in these tables includes internal, librational and lattice translational modes, and in compounds with tetrahedral moieties such as $[SiO_4]^{4-}$, the main bands are usually attributed to internal vibrations of the tetrahedra. Therefore, comparison between the number and symmetry of internal modes (in both space groups) with experimental results is probably more instructive than the total number of expected modes. The internal modes of tetrahedral anions are usually denoted using the same notation as those in isolated, perfect tetrahedra: ν_1 (symmetric stretching), ν_2 (symmetric bending), ν_3 (asymmetric stretching) and ν_4 (asymmetric bending). For free $[SiO_4]^{4-}$ these modes appear at 819 cm^{-1} (ν_1), 956 cm^{-1} (ν_3), 340 cm^{-1} (ν_2) and 527 cm^{-1} (ν_4),[37] while in rare earth silicate apatites these frequencies may vary (depending on the compositions) around the following values: $\nu_1 \sim 850$ cm^{-1}, $\nu_3 \sim 930$ cm^{-1}, $\nu_2 \sim 400$ cm^{-1}, and $\nu_4 \sim 530$ cm^{-1}.[38-41] These internal modes and symmetries are summarized in Tables S3 and S4 of the Supplementary Information. As the $Nd_{9.33}Si_6O_{26}$ single crystals were grown along the crystallographic *c* axis,[21] a transverse section coincides with the *ab* basal plane and the *c* direction is contained in a longitudinal section along the direction of crystal growth. Thus, *u* and *v* are denoted as two arbitrary but perpendicular directions within the *ab* basal plane, and *u* is perpendicular to the *c* axis in the longitudinal section (Fig. 2). Spectra were measured in backscattering configuration in these two planes, both in parallel and crossed polarizations, i. e. with the scattered electric field either parallel or perpendicular to the incident one. Fig. 3 shows Raman spectra recorded in the as-grown $Nd_{9.33}Si_6O_{26}$ single crystals in three experimental configurations: *zz* and *uz* in a longitudinal section and *uv* in a transverse section. These three spectra allow full identification of mode symmetries, giving A_g (*zz*), E_{1g} (*uz*) and E_{2g} (*uv*) modes in $P6_3/m$ space group. It should be noted that the selection rules for A, E_1 and E_2 modes in the case of $P6_3$ space group are the same as for A_g, E_{1g} and E_{2g} in $P6_3/m$. Spectra have been decomposed as a sum of bands with pseudo-Voigt profile with the aid of LabSpec software, with position, width, integrated area and Gaussian/Lorentzian mixing factor of each band used as fitting parameters. Experimental frequencies obtained for the as-grown sample are listed in Table 3. In total, 22 A_g, 21 E_{1g} and 23 E_{2g} are identified, which is significantly less than the total number of modes of 90 (30 A + 30 E_1 +30 E_2) in $P6_3$ (with split O(1), O(3) and O(4) sites as determined by neutron diffraction). On the other hand, the total number of modes in $P6_3/m$ space group (with split O(1) and O(3) sites as determined by neutron diffraction) is 51 (18 A_g + 14 E_{1g} + 19 E_{2g}), which is closer to the experimental results and the discrepancy may be attributed to the contribution of oxygen interstitials and local symmetry lowering of perturbed SiO_4 units that are to be discussed in the subsequent section. It should also be noted that O(2) has very anisotropic atomic displacement with a much larger magnitude along *c* axis direction (Table 2), and therefore this disorder could also be modeled by a O(2)' split site, which has 12*i* symmetry and thus contributes additional 9 (3 A_g + 3 E_{1g} + 3 E_{2g}) modes, making the total number of modes to be 60 (21 A_g + 17 E_{1g} + 22 E_{2g}), which is even closer to the experimental results. However, such site split is less noticeable than O(1)' and O(3)' as it splits along the shorter *c* axis, and it can also be effectively modeled using anisotropic displacement parameters. (In fact, in order to minimize the number of parameters to improve the data refinement stability, we choose to split only O(3) site in Table 4.) It can be therefore concluded that

$Nd_{9.33}Si_6O_{26}$ is consistent with $P6_3/m$ space group, instead of $P6_3$. Compared to our previous Raman study of $Nd_8Sr_2Si_6O_{26}$,[25] whose experimental results fit very well with $P6_3/m$ without any oxygen split sites, the additional Raman modes in $Nd_{9.33}Si_6O_{26}$ are thus attributed to the disorders at oxygen sites and interstitials introduced by cation vacancies, instead of long-range symmetry lowering to $P6_3$.

Neutron diffraction allowed the detection of Frenkel-type defects with oxygen entering interstitial positions along the [001] channel center (O(6) in $P6_3$ and O(5) in $P6_3/m$). Tables 4 and 5 list the atomic positions and displacement parameters of undoped $Nd_{9.33}Si_6O_{26}$ over a range of temperatures from the Laue diffraction data. However, the signals from interstitial positions are weaker than the O(3)' split sites, and their occupancies could not be successfully refined. Nonetheless, their existence is unequivocal from Fourier mapping (Fig. 4) that permits positional specification and provides an estimate of concentration (Table 6). There was little temperature dependence on the abundance of oxygen interstitials from 4K to room temperature, but the number of detected sites varied from 4-9, with the highest number found for 773K (Fig. 5). The interstitial positions also vary with temperature, and while the interstitial oxygen resident in the tunnel is very close (0.001-0.003Å) to the *c* axis from 4 – 300K, it becomes displaced from the channel center at elevated temperatures (0.69Å at 573K and 0.54Å at 773K). In addition, new interstitial sites appear in the tunnel at 573K and between the SiO_4 tetrahedra at 773K.

It should be noted that these oxygen interstitials could also contribute additional Raman modes. Table S5 in Supplementary Information summarizes Raman activity that oxygen interstitials may contribute, based on their positions and symmetries. The interplay between cation vacancies, oxygen sublattice distortion and Raman spectra can be better elucidated by careful study of [SiO_4] internal modes, which are expected to be very sensitive to split oxygen sites and Si-O distances. The region of stretching modes (> 800 cm-1) is especially informative due to absence of overlapping with other lattice modes. Fig. 6 shows the decomposition of *zz* (A_g), *uz* (E_{1g}) and *uv* (E_{2g}) spectra for the as-grown $Nd_{9.33}Si_6O_{26}$ in this region, from which 6 A_g, 6 E_{1g} and 6 E_{2g} bands are identified, which are clearly more than expected from ν_1 and ν_3 bands altogether (Table S4). This discrepancy is due to the fact that in Table S4, only one single type of SiO_4 tetrahedra is assumed in which all Si environments are identical and each SiO_4 group consists of only four oxide ions. In reality, the split of oxygen sites leads to (at least) two types of SiO_4 tetrahedra, either perturbed or unperturbed by the presence of adjacent Nd vacancies. The multiplication of internal modes due to the existence of different types of SiO_4 tetrahedra is clearly manifested in the high frequency *zz* spectrum (Fig. 6(a)), whose ν_1 band consists of two main components at ~852 and ~861 cm^{-1} and a third, weaker one at ~880 cm^{-1}. The appearance of two A_g breathing modes is not compatible with the expectations for a single type of tetrahedra (Table S4) and requires the assumption of multiple environments for Si. In fact, symmetry lowering to $P6_3$ would neither explain this result, as it also predicts only one A mode in the ν_1 region (Table S3). In the assumption that the two main components of ν_1 are due to two types of tetrahedra, namely those perturbed or unperturbed by adjacent vacancies, we may relate the intensities of those bands to the proportion of the two types of tetrahedra and compare with predictions in accordance with the vacancy concentration. It should be noted that the intensities depend largely on the conditions imposed to the fitting parameters, with representative values being I(854)/Sum = 0.3±0.07. Here, the low frequency components are assigned to the unperturbed tetrahedra and high frequency ones to the perturbed tetrahedra, in agreement with the proposal made by Guillot et al.,[37] who stated that a vacancy at the Nd(1) site would push the neighboring oxygen atoms away, thus shortening the Si-O bonds and resulting in frequency increase for the breathing mode. Our attribution is also in agreement with the observations made by Wu et al. in $RE_{9.33}(SiO_4)_6O_2$ apatites where the splitting of the ν_1 mode was seen to increase with decreasing ionic radius of the rare earth cation.[41] Within this hypothesis the ratio between the Raman intensities fits rather well with the populations of unperturbed and perturbed tetrahedra as derived from the concentration of Nd(1) vacancies and the number of neighboring tetrahedra (six), which yield a theoretical ratio of about 1/3 to 2/3 between them.

However, while the assumption of two types of SiO_4 tetrahedra explains the results for A_g and E_{2g} symmetries, a clear discrepancy remains in the number of E_{1g} modes. In particular, no E_{1g} mode is expected in the ν_1 region and only two in the ν_3 region, which is far from the six experimentally observed in *uz* geometry. This discrepancy could be attributed to a local symmetry lowering of the perturbed SiO4 units from C_s to C_1 when split oxygen sites are considered in the Si environment with O(1)' and O(2)' out of the mirror plane. As shown in Table S6, symmetry lowering to C_1 for SiO4 yields a splitting of ν_1 as $A_g + E_{1g} + E_{2g}$, which explains the detection of an E_{1g} mode in the ν_1 region, as well as extra E_{1g} modes in the ν_3 region.

Still, things are less clear for ν_2 and ν_4 bands, due to the fact that other modes (mainly channel and interstitial oxygen vibration) may overlap with them. In total, 3 A_g, 4 E_{1g} and 5 E_{2g} are identified in the ν_2 region around 400 cm^{-1} and 4 A_g, 4 E_{1g} and 4 E_{2g} in the ν_4 region around 530 cm^{-1}, which could also be attributed to oxygen site split and local symmetry lowering.

The lattice and atomic parameters of Al-doped $Nd_{(28+x)/3}Al_xSi_{6-x}O_{26}$ (x = 0.5, 1.0 and 1.5) are listed in Tables 7 and 8. As Al^{3+} (IR = 0.39Å)[42] is larger than Si^{4+} (0.26Å)[42], both *a* and *c* increase as the crystals become more aluminous. For the dilated unit cell, steric hindrance towards oxygen migration is reduced. The O(3) order was also improved, reflected in less occupancy at the O(3)' split site as x increases. Fig. 7 shows the distribution of the interstitial sites at 100K for $Nd_{(28+x)/3}Al_xSi_{6-x}O_{26}$ (x = 0.5, 1.0 and 1.5), with their locations and concentrations listed in Table 9. As the crystals become more aluminous, the abundance of interstitials is reduced ($2Si^{4+} + O_i^{2-} \rightarrow 2Al^{3+}$

+ $\square_i$) and the interstitials originating in tunnel move towards the framework, while simultaneously the Nd^F vacancy concentration decreases ($\square_{Nd} + 3Si^{4+} \rightarrow Nd^{3+} + 3Al^{3+}$). At x = 1.5, the tunnel is devoid of interstitials, which are then located in the framework.

To better correlate crystal chemistry with functionality, samples with poorer conductivity were also examined. Table 10 and 11 list the atomic positions and displacement parameters of the undoped $Nd_{9.33}Si_6O_{26}$ that has been annealed for 3 months at 950°C as compared with the as-grown crystal. For better calculation and display of interstitial positions, splitting of oxygen sites other than O(3)' are not included during data fitting, resulting in a poorer GOF for the undoped $Nd_{9.33}Si_6O_{26}$ to the $P6_3/m$ model at room temperature. Overall, the annealed crystal is better ordered, as O(4) is fully occupied and the Nd(1) occupancy is closer to the ideal value (0.833) per formula unit. The interstitial positions and concentrations at Fourier peaks of $Nd_{9.33}Si_6O_{26}$ (prior to and after annealing) are illustrated in Fig. 8 and collated in Table 12. In an analogous fashion to Al-doping, the tunnel interstitials in $Nd_{9.33}Si_6O_{26}$ migrate towards the framework after annealing, but the overall concentration of interstitials is significantly lower. This may be due to the presence of Si_2O_7 dimers in the framework[43] and the subsequent elimination of interstitials ($O_i^{2-} + Si_2O_7^{6-} \rightarrow 2SiO_4^{4-}$) after heat treatment.

Fig. 9 shows the Raman spectra of the annealed $Nd_{9.33}Si_6O_{26}$ crystal (950°C/3 months) in *zz*, *uz* and *uv* configurations. Raman shifts obtained by profile decomposition are listed in Table 13. While the spectra look similar in both samples, there are small but significant differences in the high frequency region, specifically in the relative proportion of the bands composing the breathing ν_1 mode with A_g symmetry. Profile fitting (Fig. 10) yields clearly three components at frequencies close to those of the as-grown crystal but with smaller linewidths and different relative intensities. The third component, in particular, is considerably enhanced at the expense of the second one. The ratio between the area of the first component and the integrated area of the whole ν_1 band is, however, quite similar to that found for the as-grown sample with a slight decrease. It should be noted that while fitting spectra with overlapping bands is subject to large errors, such an increase in the third band is beyond fitting errors and thus associated with structural features instead. Since the major difference between these two samples is the shift of the oxygen interstitials in the annealed sample from the channel axis towards a peripheral 6*h* site close to SiO_4 tetrahedra, it is suggested that the third band arises from tetrahedra perturbed by peripheral O_{int}. These ions are not close enough to Si so as to yield a SiO_5 entity, but may have an effect on oxygen bonding by pushing O3 ions to split O(3)' sites with shorter Si-O bond distances (and thus higher frequencies). This is supported by a slight increase of the significant figures of O(3)' in the annealed sample as compared to the as-grown one (Table 10).

It should also be noted that the discrepancy in the number of E_{1g} modes at high frequency remains in the annealed crystal, which supports our interpretation that it has an intrinsic origin, such as the local symmetry lowering of the SiO_4 unit due to split oxygen sites around cation vacancies. At lower frequencies, differences are suggested to be due to the disappearance of O_{int} in the channel axis and its shift to a new site in the periphery. Specifically, as Table 13 shows, one band of each symmetry type should disappear, but no clear evidence is found of any modes disappearing in the annealed crystal that might be attributed to the O_{int} at 4*e* site. This may be due to several causes: (1) it is possible that those O_{int}, though at 4*e* site on average, are in fact highly disordered along the *c* axis, which may broaden the bands and make them indistinguishable from the background; (2) these Oint are so close to the origin at room temperature that they can be better described as occupying the 2*b* site (000), which has inversion symmetry and is thus not Raman active (Table S5). On the other hand, new bands should be observed in the annealed sample arising from the interstitial oxide ions at the channel periphery. The enhancement of bands at ~290 and ~330 cm^{-1} in *zz* and at ~260 and ~350 cm^{-1} in *uz* could be assigned to these interstitial oxygen atoms, though their symmetries do not fully agree with expectations from an extra 6*h* site.

■ DISCUSSION

Computational approaches suggest two conduction pathways for interstitial oxygen: (i) directly along the *c* axis tunnel center with O^{2-}, progressing through adjacent interstitial sites including residence at the O(4) position;[9,16] or (ii) across the *ab* basal plane, where mobility is facilitated by the presence of Nd^F framework interstitials,[14,17] or realized through tilting of SiO_4 tetrahedra.[15] Here, the first direct observation of interstitial O^{2-} is consistent with transportation pathways involving O(4) and two O(3) (Fig. 11). The interstitials enable horizontal (*ab* plane) conduction from O(3) to the tunnel O(4) locations, together with vertical routes (*c* axis) between the two O(3) of the SiO_4 tetrahedron. In combination, these mechanisms show oxygen migration is best considered a whole-of-crystal percolation. The interstitial positions confirm two alternate migration paths along the tunnel, and facilitate conduction between the SiO_4 tetrahedra through the tunnel walls, in a manner similar to $La_{9.69}Si_{5.70}Mg_{0.30}O_{26.24}$.[44] The Laue diffraction data of undoped $Nd_{9.33}Si_6O_{26}$ collected at 4K reveals the void space within the lattice (Fig. 12), through which migration of oxygen takes places along [001].

When undoped $Nd_{9.33}Si_6O_{26}$ is heated towards the SOFC operating temperature (500-700°C), the putative 4*e* interstitials shift to locations near the c axis with 12*i* symmetry (Fig. 5), and ionic conductivity is steadily enhanced as interstitial concentration increased. At 573K, more interstitial sites become available within the tunnel and a dual-conduction path is created at 773K. This boosts conductivity and correlates with the inflection evident in the [001] log(σT) against 1/T plots.[45] This feature is, however, absent after annealing as the *c*-axis interstitials move away from the tunnel, the split conduction routes cannot form, and conductivity is lowered.

For Al-doped $Nd_{(28+x)/3}Al_xSi_{6-x}O_{26}$, the tunnel interstitials also move further into the framework as *x* increases (Fig. 7). With the dual-conduction path removed, the ionic conductivity along *c* axis decreases as the crystal becomes more aluminous. However, as the interstitials enter the framework, the oxygen mobility across *ab* basal plane is enhanced. Also, without increased tunnel interstitials at elevated temperature, no inflection has been observed in the conductivity plots of these Al-doped crystals.[22]

■ CONCLUSION

Neutron diffraction with Laue and fixed wavelength four-circle methods was performed on single crystals of $Nd_{(28+x)/3}Al_xSi_{6-x}O_{26}$ (x = 0, 0.5, 1.0 and 1.5) and provided comparable structure solutions. All Laue diffraction data fitted $P6_3/m$. Compared with single crystal X-ray diffraction of Al-doped apatites,[22] Laue diffraction yielded an improved GOF when the O(3) site is split and better definition of the large cation displacement parameters. While treatment of Laue diffraction data of undoped $Nd_{9.33}Si_6O_{26}$ collected at 2K shows a slightly better GOF with $P6_3$, primarily due to better fitting of Nd^F vacancy distribution, the evidence is not sufficiently compelling to discard the $P6_3/m$ model (at least for the materials used). A separate study with Raman spectroscopy also confirmed the as-grown $Nd_{9.33}Si_6O_{26}$ crystal to have $P6_3/m$ symmetry. Raman work also confirmed the split of oxygen sites, though O(1)' and O(2)' can also be modeled by large anisotropic atomic displacements.

The direct observation of oxygen interstitials shows for the first time the different modalities connecting the tunnel O(4) to the framework SiO_4 tetrahedra via O(3) atoms, that facilitates ionic conduction in two principal directions.

(i) For O^{2-} migration along [001], this conduction path can serve as an alternate route, in addition to those deduced from computational studies.[9,16,17] For undoped $Nd_{9.33}Si_6O_{26}$, it was also found that additional tunnel interstitials become available at 573-773K, which enhances the O^{2-} transport and results in the distinctive inflection in the conductivity plot against temperature. This structural change takes place at intermediate temperatures, and should prove beneficial when oxyapatites are deployed in SOFC.

(ii) For O^{2-} transport perpendicular to [001], inter-tunnel conduction provides an auxiliary diffusion pathway within the framework structure realized by lattice cavities revealed by this work, interstitials,[17] and probably exchange processes involving the formation of transitory Si_2O_9 dimers,[15] Such exchange processes are supported by the observation from ^{17}O NMR studies of the ready exchange of the oxide ions of the Si/GeO_4 groups.

The tunnel interstitials shift towards the framework when the crystal is doped with Al or subjected to long-term annealing. With the dual-conduction path disabled, O^{2-} migration along the *c* axis is very well described by previously published mechanisms derived from simulation and mobility is thus attenuated. This change is reflected in the removal of the inflection in the conductivity plot. However, for Al-doped series $Nd_{(28+x)/3}Al_xSi_{6-x}O_{26}$, the ionic conductivity across *ab* basal plane increases as these interstitials move into the framework. This is consistent with earlier magic angle spinning nuclear magnetic resonance (MAS NMR) studies,[39,46] that showed stoichiometric $La_8Sr_2Si_6O_{26}$ displayed a single resonance corresponding to the SiO_4 group, while in $La_9SrSi_6O_{26.5}$ containing excess oxygen, an additional resonance associated with interstitial oxygen adjacent to SiO_4 (i.e. SiO_5) was observed. This experimental determination of interstitial distribution and discovery of the dual-conduction path at intermediate temperatures provides a systematic understanding of oxide migration in oxyapatites, and these insights can guide future performance optimization.

■ ASSOCIATED CONTENT

Single crystal neutron diffraction data in Crystallographic Information File (CIF) format. This material is available free of charge via the Internet at http://pubs.acs.org.

AUTHOR INFORMATION

Corresponding Author

* Email: tjwhite@ntu.edu.sg; jwei@simtech.a-star.edu.sg.

Notes

The authors declare no competing financial interest.

ACKNOWLEDGMENT

We are pleased to acknowledge the Agency for Science, Technology and Research (A*STAR) PSF grant 082 101 0021 'Optimization of Oxygen Sublattices in Solid Oxide Fuel Cell Apatite Electrolytes' for funding the work and the Ministry of Education (MOE) Tier 2 grant T208B1212 for enabling the purchase of a single crystal X-ray diffractometer.

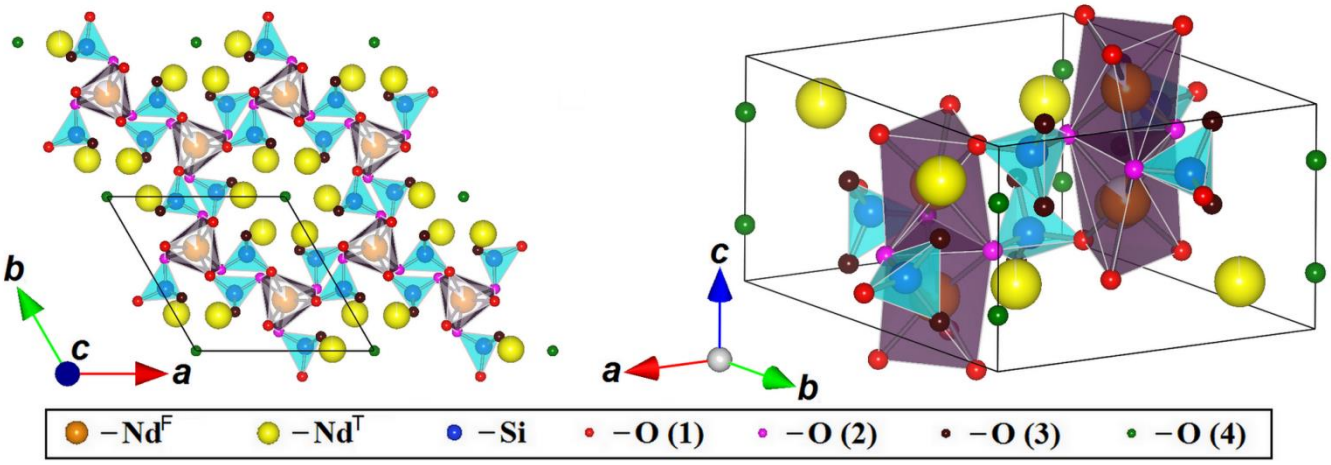

Figure 1. The apatite structure of $Nd_{9.33}Si_6O_{26}$ with $P6_3/m$ symmetry. The Nd(1) (Nd^F) atoms occupy the framework sites (4*f*) and its occupancy is represented by the filled area of the sphere. Each Nd(1) forms a Nd^FO_6 metaprism with three O(1) atoms (6*h*) and three O(2) atoms (6*h*). A framework structure is formed when these metaprisms are corner-connected to SiO_4 tetrahedra (with centered Si (6*h*) bonded to one O(1) (6*h*), one O(2) (6*h*) and two O(3) atoms (12*i*)). This framework surrounds the Nd (2) (Nd^T) atoms (6*h*), which in turn enclose the O (4) atoms (2*a*) located along the *c* axis tunnel.

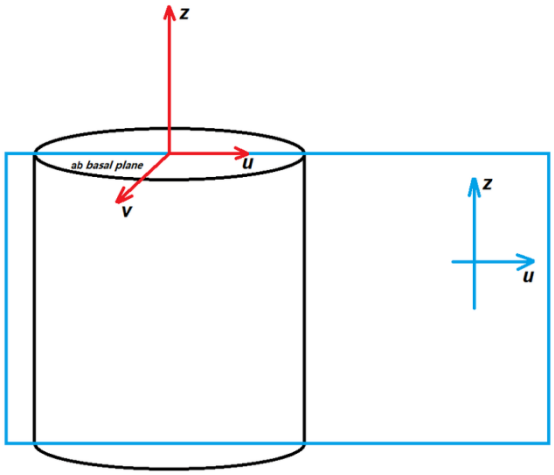

Figure 2. Schematic diagram showing the configurations of the Raman measurements. *u* and *v* are two perpendicular directions in the *ab* basal plane and *u* is perpendicular to *z*, which is along the crystallographic c axis. Under this configuration, the *uv*, *zz* and *uz* spectra correspond to E_{2g}, A_g and E_{1g} symmetries, respectively.

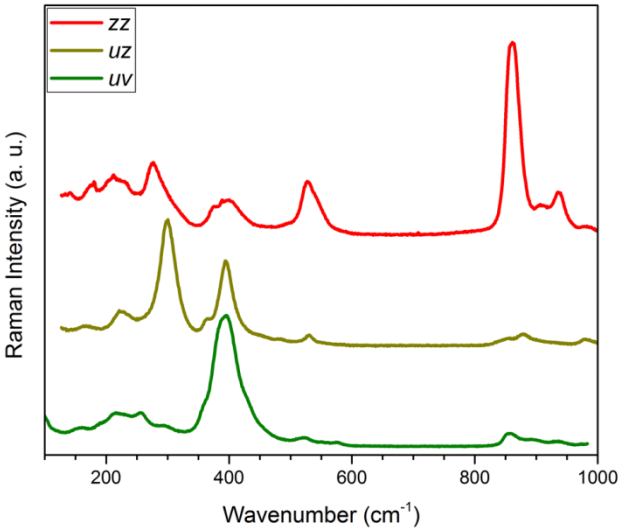

Figure 3. Raman spectra of as-grown $Nd_{9.33}Si_6O_{26}$ single crystal collected at room temperature.

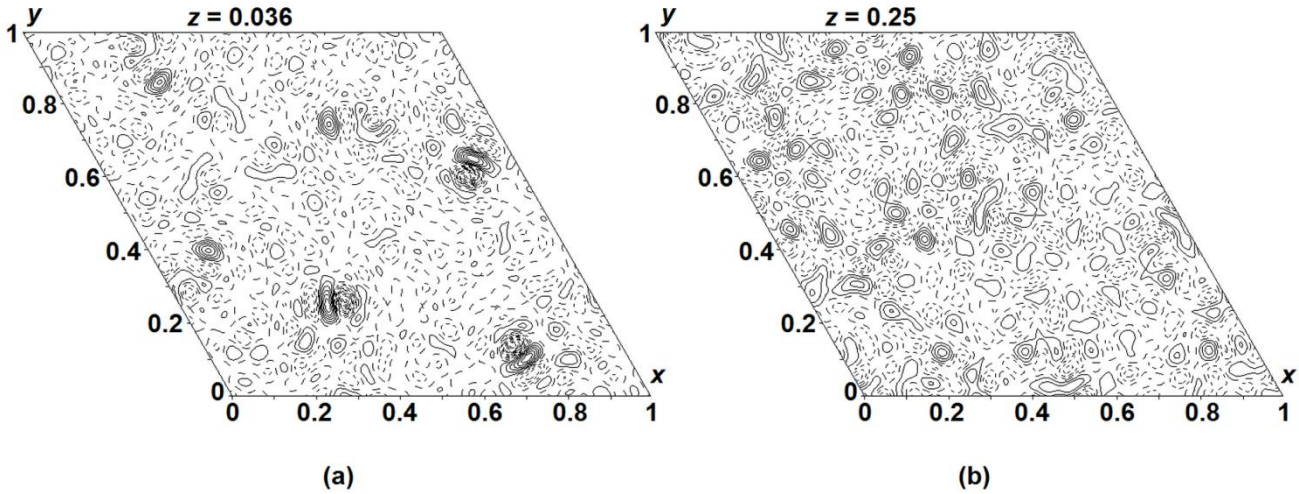

Figure 4. Representative difference Fourier maps obtained from the as-grown $P6_3/m$ $Nd_{9.33}Si_6O_{26}$ crystal with neutron diffraction data collected at (a) 4K and (b) 773K. Locations with closely spaced contours reflect the positions of interstitial oxygen. The step size of the positive (solid line) and negative (dotted line) contours is 0.5 fm.

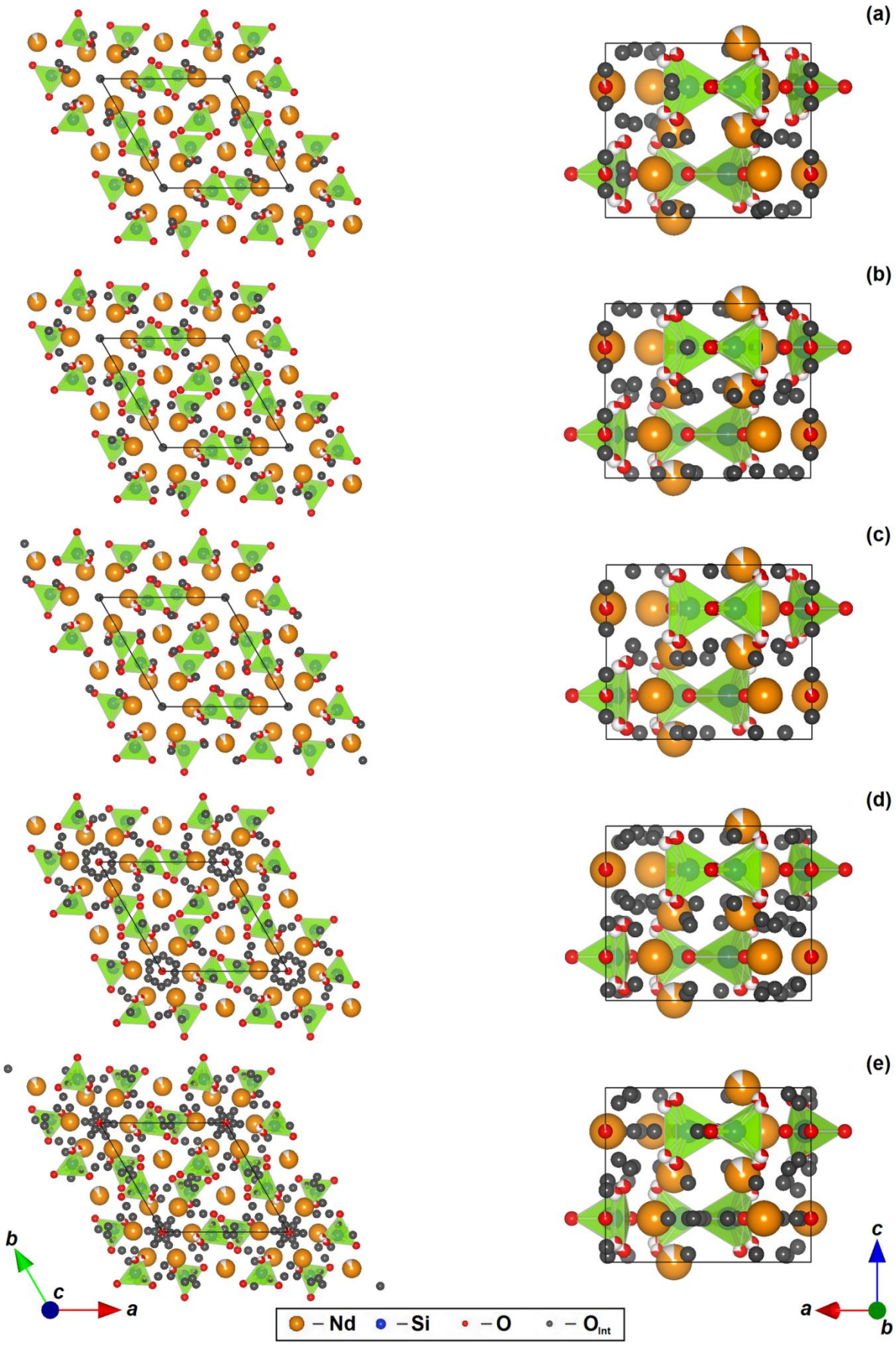

Figure 5. The concentration and distribution of oxygen interstitials in $P6_3/m$ $Nd_{9.33}Si_6O_{26}$ at (a) 4K (b) 100K (c) 300K (d) 573K and (e) 773K viewed along [001] (left) and [010] (right).

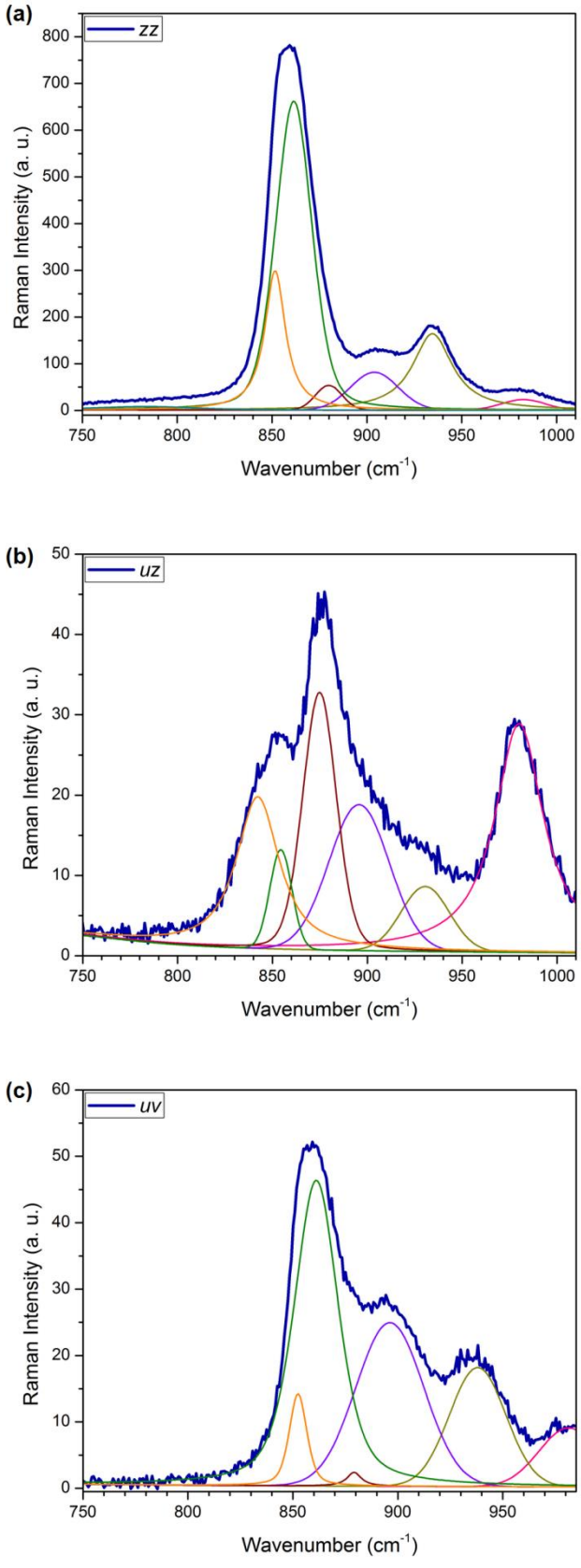

Figure 6. Profile fitting of the (a) *zz*, (b) *uz* and (c) *uv* spectra of the sa-grown $Nd_{9.33}Si_6O_{26}$ single crystal in the region of ν_1 and ν_3 internal modes of SiO_4 tetrahedra.

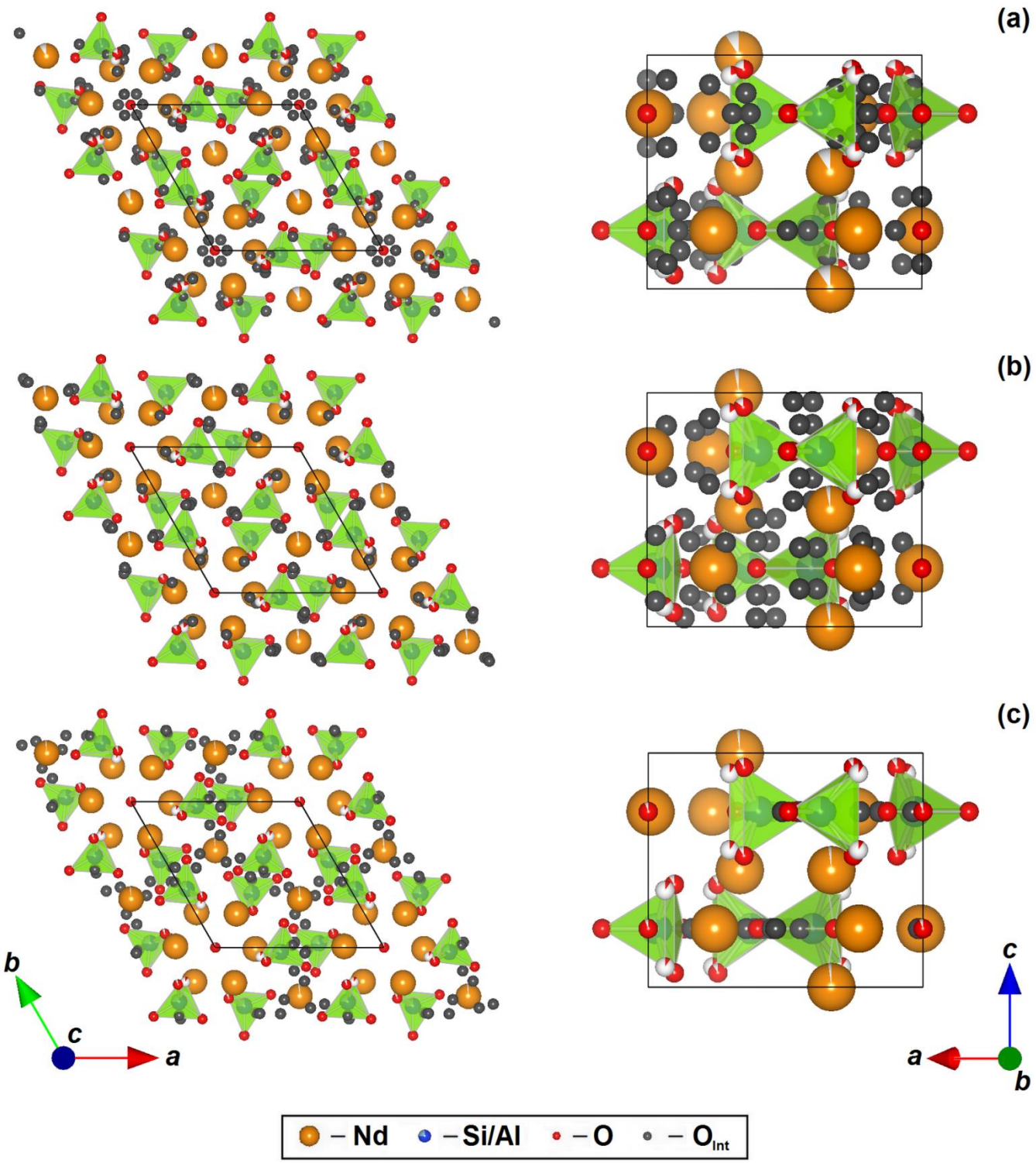

Figure 7. The concentration and distribution of oxygen interstitials at 100K in $P6_3/m$ $Nd_{(28+x)/3}Al_xSi_{6-x}O_{26}$ with (a) x = 0.5, (b) x = 1.0 and (c) x = 1.5 viewed along [001] (left) and [010] (right). The occupancy of each element is represented by the filled area of the sphere.

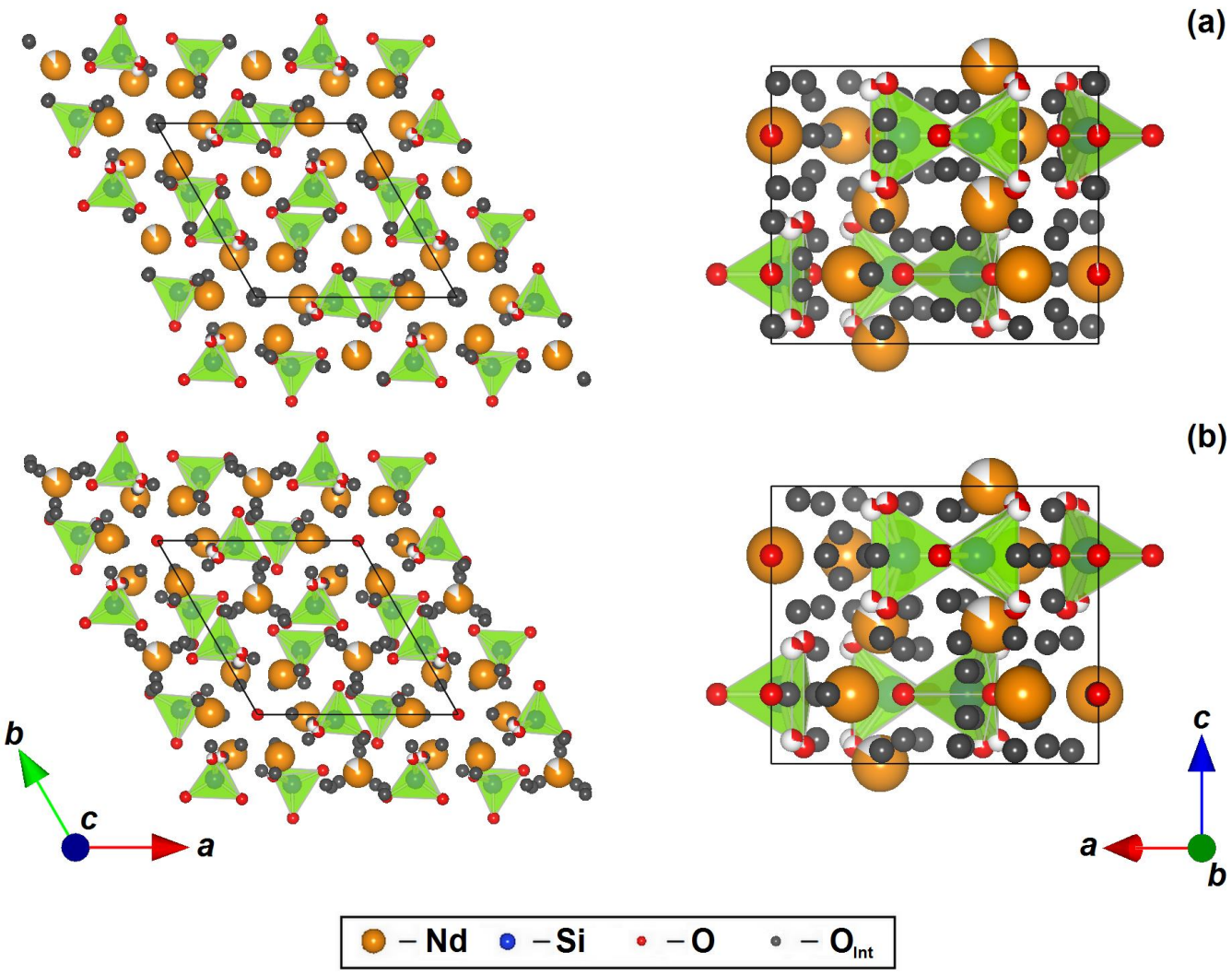

Figure 8. The concentration and distribution of oxygen interstitials in (a) as-grown $Nd_{9.33}Si_6O_{26}$ and (b) annealed $Nd_{9.33}Si_6O_{26}$ at room temperature viewed along [001] (left) and [010] (right).

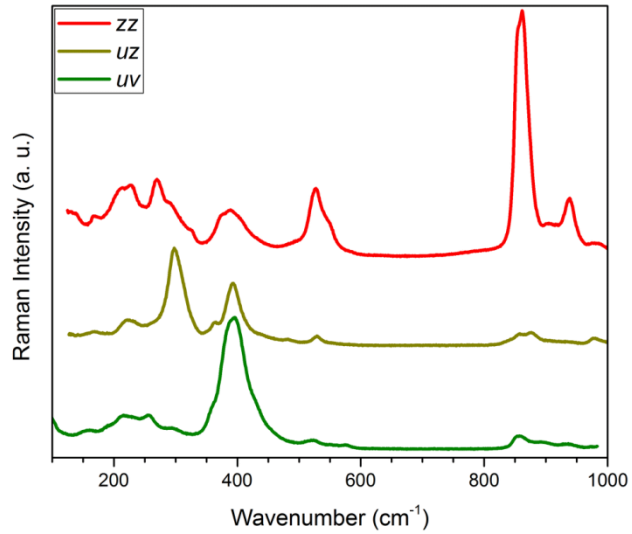

Figure 9. Raman spectra of the annealed $Nd_{9.33}Si_6O_{26}$ single crystal.

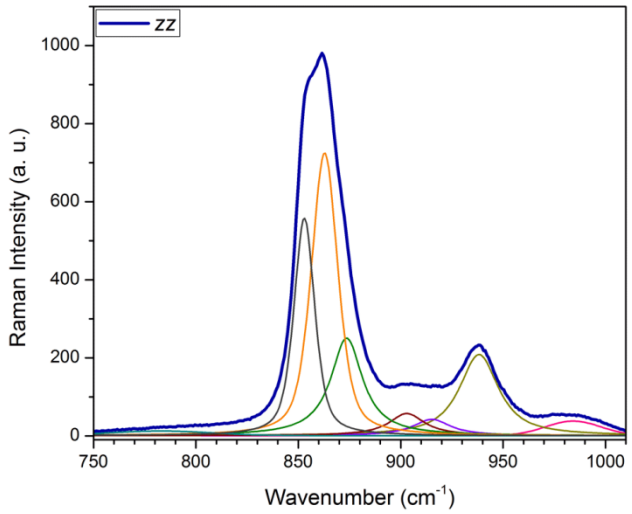

Figure 10. Profile fitting of the *zz* spectrum of the annealed $Nd_{9.33}Si_6O_{26}$ single crystal in the region of ν_1 and ν_3 internal modes of SiO_4 tetrahedra.

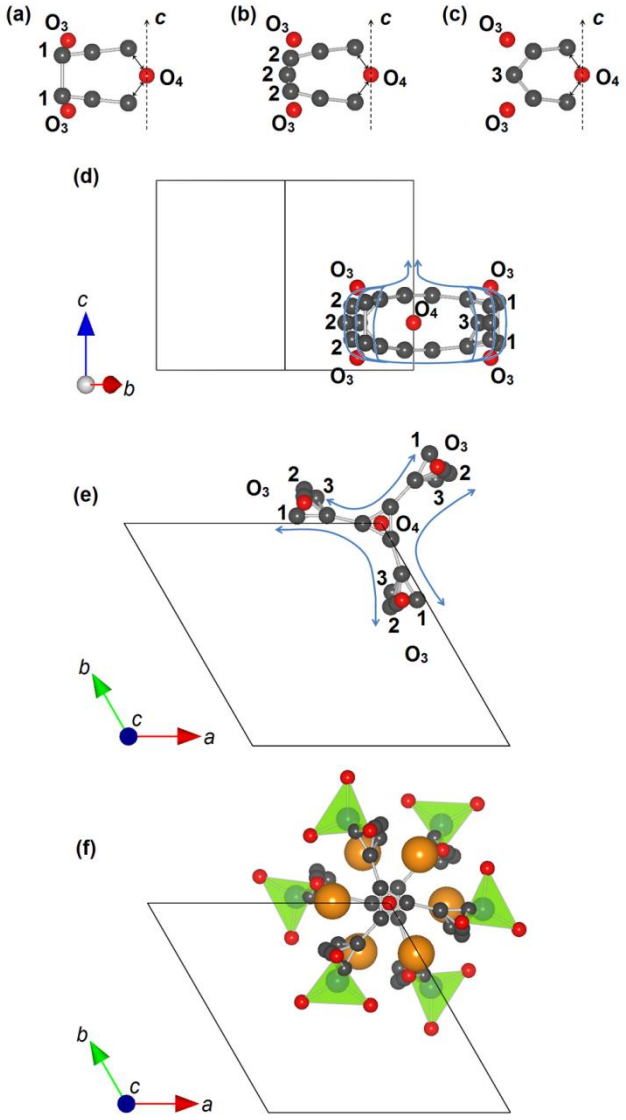

Figure 11. The O^{2-} conduction paths around the tunnel centered at (00z) deduced from neutron diffraction, which become effective at intermediate SOFC operating temperature. Oxygen may migrate horizontally between O(4) and O(3) through the interstitial sites (grey color), and vertically between O(3) atoms through 3 possible interstitial paths ((a) – (c)). O^{2-} may thus (d) move along [001] or (e) diffuse in (001) across the tunnel via these transport routes. (f) Per unit cell, there are six SiO_4 tetrahedra, and each has dual-conduction path connected to the tunnel.

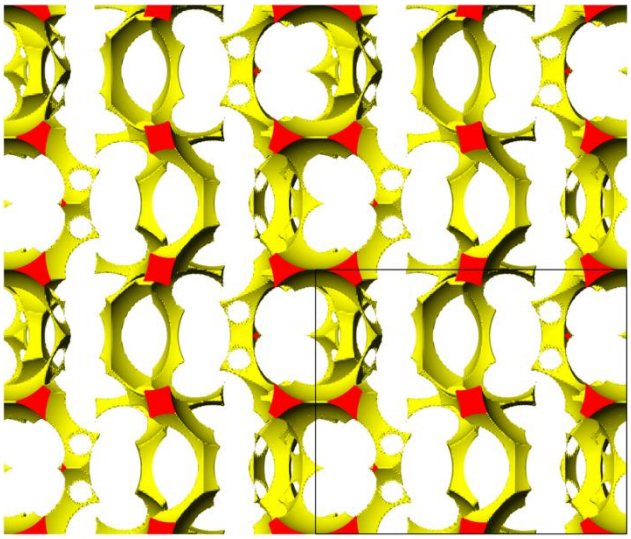

Figure 12. Atomic void space (viewed along [010]) as calculated from Laue diffraction solution of $Nd_{9.33}Si_6O_{26}$ collected at 4K where the oxygen interstitials are excluded. This representation emphasizes the possible locations of extra-stoichiometric oxygen and the migration path of O^{2-}.

Table 1. Refined atomic positions and displacement parameters of $Nd_{9.33}Si_6O_{26}$ from fixed wavelength diffraction data collected at 2K using the $P6_3$ model, which enables the specification of the framework cation vacancy distribution to be solely at 2*b* Nd(1) site. This leads to a slightly improved fit (GOF: 1.97, R: 3.07% and Rw: 2.97%) as compared to $P6_3/m$ model.

Atom	Wyckoff	Occupancy	x	y	z	U11	U22	U33	U12	U13	U23
Nd(1)	2b	0.75	0.3333	0.6667	-0.012(1)	0.0038(5)	0.0038(5)	0.0069(7)	0.0019(3)	0	0
Nd(2)	2b	1	0.6667	0.3333	-0.011(1)	0.0049(4)	0.0049(4)	0.035(1)	0.0024(2)	0	0
Nd(3)	6c	1	0.23032(4)	-0.01049(4)	0.241(1)	0.0056(1)	0.0030(1)	0.0051(1)	0.00220(9)	-0.0005(4)	0.0001(4)
Si	6c	1	0.40121(7)	0.37203(7)	0.241(1)	0.0063(2)	0.0050(2)	0.0048(2)	0.0037(2)	0.0012(8)	-0.0006(7)
O(1)	6c	0.78(1)	0.3268(3)	0.4916(3)	0.243(1)	0.0147(6)	0.0108(6)	0.0077(4)	0.0103(5)	0.0002(7)	-0.0035(7)
O(1)'	6c	0.22(1)	0.2945(9)	0.4581(8)	0.215(1)	0.0147(6)	0.0108(6)	0.0077(4)	0.0103(5)	0.0002(7)	-0.0035(7)
O(2)	6c	1	0.59736(6)	0.47398(6)	0.240(1)	0.0073(2)	0.0069(2)	0.0183(3)	0.0010(2)	0.0001(7)	0.0045(7)
O(3)	6c	0.76(1)	0.3571(6)	0.2576(3)	0.052(1)	0.017(1)	0.0153(8)	0.0049(6)	0.012(1)	-0.0026(8)	-0.0025(6)
O(3)'	6c	0.24(1)	0.308(2)	0.242(1)	0.070(2)	0.017(1)	0.0153(8)	0.0049(6)	0.012(1)	-0.0026(8)	-0.0025(6)
O(4)	6c	0.737(7)	0.3506(4)	0.2529(3)	0.428(1)	0.011(1)	0.0050(6)	0.0068(7)	0.0044(7)	0.0031(7)	0.0016(5)
O(4)'	6c	0.263(7)	0.3012(11)	0.2442(7)	0.402(1)	0.011(1)	0.0050(6)	0.0068(7)	0.0044(7)	0.0031(7)	0.0016(5)
O(5)	2a	0.87(4)	0	0	0.243(1)	0.0074(5)	0.0074(5)	0.035(4)	0.0037(3)	0	0
O(6)	2a	0.16(4)	0	0	0.15(1)	0.026(5)	0.026(5)	0.06(3)	0.013(2)	0	0

Table 2. Refined atomic positions and displacement parameters of $Nd_{9.33}Si_6O_{26}$ from fixed wavelength diffraction data collected at 2K using the $P6_3/m$ model. The fit is slightly inferior (GOF: 2.37, R: 3.56% and Rw: 3.47%) as compared to the $P6_3$ model, but for the present crystals best represents the average symmetry.

Atom	Wyckoff	Occupancy	x	y	z	U11	U22	U33	U12	U13	U23
Nd(1)	4f	0.859(4)	1/3	2/3	-0.0009(1)	0.0042(2)	0.0042(2)	0.0201(3)	0.00211(9)	0	0
Nd(2)	6h	1	0.01049(5)	0.24082(5)	0.01049(5)	0.0031(2)	0.0043(2)	0.0051(2)	0.0009(1)	0	0
Si	6h	1	0.40128(9)	0.37210(9)	0.40128(9)	0.0066(3)	0.0053(3)	0.0048(3)	0.0038(2)	0	0
O(1)	6h	0.70(2)	0.3287(5)	0.4938(5)	0.3287(5)	0.0109(9)	0.0067(10)	0.0068(4)	0.0064(9)	0	0
O(1)'	12i	0.139(8)	0.2978(9)	0.4608(9)	0.2282(8)	0.0109(9)	0.0067(10)	0.0068(4)	0.0064(9)	0	0
O(2)	6h	1	0.59729(7)	0.47399(7)	0.59729(7)	0.0075(2)	0.0068(2)	0.0176(3)	0.0010(2)	0	0
O(3)	12i	0.753(3)	0.35337(12)	0.25487(8)	0.0618(1)	0.0155(4)	0.0103(2)	0.0058(2)	0.0086(2)	-0.0030(2)	-0.0022(2)
O(3)'	12i	0.247(3)	0.3038(4)	0.2437(3)	0.0851(3)	0.0155(4)	0.0103(2)	0.0058(2)	0.0086(2)	-0.0030(2)	-0.0022(2)
O(4)	2a	0.88(3)	0	0	1/4	0.0075(5)	0.0075(5)	0.037(3)	0.0038(3)	0	0
O(5)	4e	0.08(2)	0	0	0.15(1)	0.036(8)	0.036(8)	0.06(3)	0.018(4)	0	0

Table 3. Raman shifts (cm^{-1}) of as-grown $Nd_{9.33}Si_6O_{26}$ single crystal derived from profile fitting of *zz*, *uz* and *uv* spectra, yielding A_g, E_{1g} and E_{2g} modes, respectively.

A_g modes	E_{1g} modes	E_{2g} modes	Assignment
107	96.3	99	Lattice and librational modes
128.4	162.7	113	
139.3	182.4	161.5	
172.6	220	192.5	
206	242	213.4	
231	264.2	233.8	
248.5 vw	298	259	
271.7		293.6	
286.8 b		329.5	
317 b			
371 b	361.8	361.5	ν_2 and other oxygen vibrations
396.3	392.6	381.4	
456.8 vb	415	400	
	442 vb	430	
	484	457 vb	
500 vb	512 vw	492 wb	ν_4 and other oxygen vibrations
523.6	528.2	524.8	
539.4	542 vb	555	
		578	
851.6	842.2	852.4	ν_1 and ν_3
861.4	854.4	861.1	
880	874.8	896.2	
904	895.7	938	
934.6	930.5	981.3	
982.5	980		
Total: 22	21	23	

Table 4. Refined atomic parameters from Laue neutron diffraction of $P6_3/m$ $Nd_{9.33}Si_6O_{26}$ as a function of temperature.

Temperature (K)	4	100	300	573	773
GOF	1.95	2.02	1.74	1.99	1.94
R (%)	5.72	6.67	6.55	12.43	12.87
R_w (%)	8.00	4.53	3.86	5.56	5.44
Nd(1), 4*f*, ($^1/_3$ $^2/_3$ z)					
z	-0.0009(1)	-0.0009(1)	-0.0007(1)	-0.0002(2)	-0.0002(2)
Occupancy	0.901(4)	0.895(5)	0.888(5)	0.902(6)	0.892(6)
U_{iso} ($Å^2$)	0.0098(2)	0.0112(3)	0.0129(2)	0.0180(4)	0.0208(4)
Nd(2), 6*h*, (*x y* $^1/_4$)					
x	0.01016(6)	0.01024(7)	0.01026(6)	0.01020(9)	0.01028(9)
y	0.24023(6)	0.24016(7)	0.23985(6)	0.2391(1)	0.2388(1)
U_{iso} ($Å^2$)	0.0041(2)	0.0053(2)	0.0078(2)	0.0129(3)	0.0162(3)
Si, 6*h*, (*x y* $^1/_4$)					

x	0.4014(1)	0.4015(1)	0.4016(1)	0.4015(2)	0.4017(2)
y	0.3723(1)	0.3723(1)	0.3725(1)	0.3727(2)	0.3728(2)
U_{iso} (Å^2)	0.0046(3)	0.0052(3)	0.0068(3)	0.0103(4)	0.0127(4)
O(1), 6*h*, (*x y* $^1/_4$)					
x	0.3232(2)	0.3228(1)	0.3231(1)	0.3235(2)	0.3235(2)
y	0.4878(1)	0.4872(1)	0.4873(1)	0.4874(2)	0.4874(2)
U_{iso} (Å^2)	0.0155(3)	0.0167(4)	0.0195(3)	0.0260(6)	0.0305(6)
O(2), 6*h*, (*x y* $^1/_4$)					
x	0.59762(9)	0.5974(1)	0.59725(9)	0.5969(2)	0.5966(2)
y	0.4740(1)	0.4738(1)	0.4736(1)	0.4734(2)	0.4731(2)
U_{iso} (Å^2)	0.0115(2)	0.0128(3)	0.0157(2)	0.0223(4)	0.0266(4)
O(3), 12*i*, (*x y z*)					
Occupancy	0.763(4)	0.763(5)	0.753(5)	0.733(9)	0.734(9)
x	0.3533(2)	0.3532(2)	0.3532(2)	0.3538(4)	0.3537(4)
y	0.2551(1)	0.2552(1)	0.2554(1)	0.2560(2)	0.2564(2)
z	0.0615(1)	0.0616(2)	0.0615(2)	0.0614(3)	0.0617(3)
U_{iso} (Å^2)	0.0096(3)	0.0111(4)	0.0139(4)	0.0198(7)	0.0246(8)
O(3)', 12*i*, (*x y z*)					
Occupancy	0.237(4)	0.237(5)	0.247(5)	0.267(9)	0.266(9)
x	0.3044(6)	0.3038(7)	0.3048(6)	0.306(1)	0.304(1)
y	0.2446(4)	0.2446(5)	0.2449(4)	0.2467(8)	0.2463(8)
z	0.0863(4)	0.0863(5)	0.0867(4)	0.0868(8)	0.0880(8)
U_{iso} (Å^2)	0.0096(3)	0.0111(4)	0.0139(4)	0.0198(7)	0.0246(8)
O(4), 2*a*, (0 0 $^1/_4$)					
Occupancy	0.895(9)	0.92(1)	0.89(1)	0.96(1)	0.95(1)
U_{iso} (Å^2)	0.0207(5)	0.0238(7)	0.0281(6)	0.046(1)	0.052(1)

Table 5. Refined anisotropic atomic displacement parameters (ADP) from Laue neutron diffraction of $P6_3/m$ $Nd_{9.33}Si_6O_{26}$ as a function of temperature.

Temperature (K)	4	100	300	573	773
Nd (1), 4*f*, (1/3 2/3 z)					
U_{11}	0.0056(3)	0.0073(3)	0.0092(3)	0.0148(4)	0.0187(4)
U_{33}	0.0183(4)	0.0191(4)	0.0205(4)	0.0245(6)	0.0249(6)
Nd (2), 6*h*, (x y 1/4)					
U_{11}	0.00268(19)	0.0038(2)	0.0063(2)	0.0112(3)	0.0143(3)
U_{22}	0.0041(2)	0.0052(3)	0.0078(2)	0.0128(4)	0.0158(4)
U_{33}	0.0043(2)	0.0055(2)	0.0078(2)	0.0125(3)	0.0160(3)
U_{12}	0.0007(2)	0.0011(2)	0.0024(2)	0.0045(3)	0.0057(3)
Si, 6*h*, (x y 1/4)					
U_{11}	0.0062(4)	0.0067(4)	0.0080(4)	0.0117(6)	0.0139(6)
U_{22}	0.0049(4)	0.0054(4)	0.0073(4)	0.0106(6)	0.0127(6)

U_{33}	0.0041(3)	0.0047(3)	0.0064(3)	0.0105(4)	0.0131(4)
U_{12}	0.0038(3)	0.0038(3)	0.0049(3)	0.0069(5)	0.0077(5)
O (1), 6*h*, (x y 1/4)					
U_{11}	0.0242(4)	0.0263(5)	0.0304(5)	0.0395(8)	0.0460(8)
U_{22}	0.0218(4)	0.0232(5)	0.0256(4)	0.0330(7)	0.0379(7)
U_{33}	0.0122(3)	0.0131(3)	0.0158(3)	0.0218(5)	0.0263(5)
U_{12}	0.0203(4)	0.0216(4)	0.0240(4)	0.0303(7)	0.0351(7)
O (2), 6*h*, (x y 1/4)					
U_{11}	0.0076(3)	0.0084(4)	0.0098(3)	0.0135(5)	0.0159(5)
U_{22}	0.0061(3)	0.0074(4)	0.0094(3)	0.0153(5)	0.0190(6)
U_{33}	0.0170(3)	0.0192(3)	0.0234(3)	0.0331(6)	0.0391(6)
U_{12}	0.0006(2)	0.0014(3)	0.0014(3)	0.0035(4)	0.0044(4)
O (3), 12*i*, (x y z)					
U_{11}	0.0170(6)	0.0196(7)	0.0241(7)	0.033(1)	0.039(1)
U_{22}	0.0108(3)	0.0122(3)	0.0152(3)	0.0217(5)	0.0261(6)
U_{33}	0.0046(3)	0.0057(3)	0.0075(3)	0.0119(5)	0.0156(6)
U_{12}	0.0097(3)	0.0110(4)	0.0136(4)	0.0188(8)	0.0219(8)
U_{13}	-0.0032(3)	-0.0040(4)	-0.0048(3)	-0.0066(7)	-0.0086(7)
U_{23}	-0.0026(2)	-0.0032(2)	-0.0040(2)	-0.0060(4)	-0.0078(4)
O (4), 2*a*, (0 0 1/4)					
U_{11}	0.0085(6)	0.0110(7)	0.0122(7)	0.020(1)	0.024(1)
U_{33}	0.045(1)	0.049(1)	0.060(1)	0.097(3)	0.109(3)

Table 6. Oxygen interstitial positions and peak concentrations from Laue neutron diffraction of $P6_3/m$ $Nd_{9.33}Si_6O_{26}$ as a function of temperature, arranged from highest to lowest concentration. Additional interstitial positions ($O_{int}3$) were detected in the tunnel at 573K and ($O_{int}1$, $O_{int}5$. $O_{int}6$) between SiO_4 tetrahedra at 773K.

	x	y	z	Conc. ($Å^{-3}$)
4K				
$O_{Int}1$	0.1429	0.3981	0.0361	0.098
$O_{Int}2$	0.0832	0.3085	0.0554	0.084
$O_{Int}3$	0.0003	0.0003	0.1539	0.081
$O_{Int}4$	0.7622	0.0851	0.2163	0.072
100K				
$O_{Int}1$	0.7302	0.1313	1/4	0.083
$O_{Int}2$	0.1431	0.4042	0.0382	0.076
$O_{Int}3$	0.0002	0.0002	0.1434	0.074
$O_{Int}4$	0.0686	0.4393	0.0279	0.071
$O_{Int}5$	0.3865	0.1276	0.024	0.071
300K				
$O_{Int}1$	0.1300	0.4034	0.037	0.074
$O_{Int}2$	0.0001	0.0001	0.1304	0.067
$O_{Int}3$	0.5079	0.1627	0.0358	0.045
573K				
$O_{Int}1$	0.1507	0.3933	0.0354	0.093
$O_{Int}2$	0.6248	0.0643	0.0557	0.088
$O_{Int}3$	0.9891	0.895	0.0596	0.088
$O_{Int}4$	0.0643	0.9214	0.0932	0.084
$O_{Int}5$	0.5911	0.8222	0.0674	0.083
773K				

$O_{Int}1$	0.5056	0.0271	1/4	0.088
$O_{Int}2$	0.2381	0.406	1/4	0.086
$O_{Int}3$	0.3575	0.4281	1/4	0.083
$O_{Int}4$	0.8912	0.0109	0.0360	0.081
$O_{Int}5$	0.4492	0.0246	1/4	0.079
$O_{Int}6$	0.0513	0.4567	1/4	0.078
$O_{Int}7$	0.1348	0.4017	0.0454	0.076
$O_{Int}8$	0.1388	0.3053	1/4	0.076
$O_{Int}9$	0.9406	0.0052	0.0875	0.076

Table 7. Refined lattice and atomic parameters from Laue neutron diffraction in $P6_3/m$ of $Nd_{(28+x)/3}Al_xSi_{6-x}O_{26}$ for x = 0.5, 1.0 and 1.5 at 100K.

x	0.5	1.0	1.5
a (Å)	9.5515	9.553	9.5611
c (Å)	7.042	7.0496	7.0607
Volume (Å^3)	556.3778	557.1533	558.9772
GOF	1.76	2.17	1.83
R (%)	9.17	6.05	6.39
R_w (%)	4.93	8.63	7.02
Nd(1),4*f*,($^1/_3$ $^2/_3$ z)			
z	0.0001 (1)	0.00012(9)	0.00021(8)
Occupancy	0.913(5)	0.977(5)	0.990(5)
U_{iso} (Å^2)	0.0118(3)	0.0111(2)	0.0073(2)
Nd(2),6*h*,(*x y* $^1/_4$)			
x	0.00997(8)	0.00944(7)	0.00844(6)
y	0.24121(9)	0.24127(7)	0.24124(6)
U_{iso} (Å^2)	0.0074(2)	0.0066(2)	0.0042(2)
Si/Al, 6*h*, (*x y* $^1/_4$)			
x	0.4010(2)	0.4014(1)	0.4016(1)
y	0.3719(2)	0.3722(1)	0.3722(1)
U_{iso} (Å^2)	0.0073(4)	0.0067(3)	0.0048(3)
O(1), 6*h*, (*x y* $^1/_4$)			
x	0.3216(2)	0.3220(1)	0.3222(1)
y	0.4874(2)	0.4888(1)	0.4896(1)
U_{iso} (Å^2)	0.0175(4)	0.0151(3)	0.0119(3)
O(2), 6*h*, (*x y* $^1/_4$)			
x	0.5988(1)	0.6006(1)	0.6020(1)
y	0.4725(1)	0.4721(1)	0.4719(1)
U_{iso} (Å^2)	0.0150(4)	0.0136(3)	0.0101(3)
O(3), 12*i*, (*x y z*)			
Occupancy	0.806(9)	0.853(7)	0.910(7)
x	0.3514(3)	0.3499(2)	0.3481(2)
y	0.2547(2)	0.2541(1)	0.2533(1)
z	0.0615(2)	0.0614(2)	0.0614(1)
U_{iso} (Å^2)	0.0133(5)	0.0123(4)	0.0104(3)
O(3)', 12*i*, (*x y* z)			
Occupancy	0.194(9)	0.147(7)	0.090(7)
x	0.3039(12)	0.301(1)	0.297(2)
y	0.2424(8)	0.2397(8)	0.236(1)
z	0.0866(9)	0.0862(9)	0.086(1)
U_{iso} (Å^2)	0.0133(5)	0.0123(4)	0.0104(3)
O(4), 2*a*, (0 0 $^1/_4$)			
U_{iso} (Å^2)	0.0250(6)	0.0212(5)	0.0158(4)

Table 8. Refined anisotropic atomic displacement parameters from Laue neutron diffraction in $P6_3/m$ of $Nd_{(28+x)/3}Al_xSi_{6-x}O_{26}$ for x = 0.5, 1.0 and 1.5 at 100K.

x	0.5	1.0	1.5
Nd (1), 4*f*, (1/3 2/3 z)			
U_{11}	0.0116(4)	0.0132(3)	0.0091(3)
U_{33}	0.0122(4)	0.0071(3)	0.0037(3)
Nd (2), 6*h*, (x y 1/4)			
U_{11}	0.0066(3)	0.0061(2)	0.0041(2)
U_{22}	0.0069(3)	0.0062(2)	0.0035(2)
U_{33}	0.0070(2)	0.0061(2)	0.0043(2)
U_{12}	0.0022(2)	0.0020(2)	0.0014(2)
Si/Al, 6*h*, (x y 1/4)			
U_{11}	0.0083(5)	0.0074(4)	0.0048(4)
U_{22}	0.0069(5)	0.0063(4)	0.0045(4)
U_{33}	0.0076(4)	0.0070(3)	0.0055(4)
U_{12}	0.0044(5)	0.0039(3)	0.0026(3)
O (1), 6*h*, (x y 1/4)			
U_{11}	0.0252(6)	0.0215(4)	0.0174(4)
U_{22}	0.0197(6)	0.0145(4)	0.0103(3)
U_{33}	0.0151(4)	0.0133(3)	0.0104(3)
U_{12}	0.0170(5)	0.0120(3)	0.0086(3)
O (2), 6*h*, (x y 1/4)			
U_{11}	0.0107(5)	0.0103(4)	0.0079(3)
U_{22}	0.0093(5)	0.0084(3)	0.0063(3)
U_{33}	0.0222(5)	0.0203(4)	0.0152(3)
U_{12}	0.0028(4)	0.0034(3)	0.0029(3)

O (3), 12*i*, (x y z)			
U_{11}	0.021(1)	0.0181(7)	0.0153(6)
U_{22}	0.0136(4)	0.0125(3)	0.0097(3)
U_{33}	0.0086(4)	0.0087(3)	0.0077(3)
U_{12}	0.0107(5)	0.0095(4)	0.0073(3)
U_{13}	-0.0041(5)	-0.0044(3)	-0.0046(3)
U_{23}	-0.0024(3)	-0.0020(2)	-0.0015(2)
O (4), 2*a*, (0 0 1/4)			
U_{11}	0.0136(7)	0.0111(5)	0.0082(4)
U_{33}	0.048(1)	0.042(1)	0.0310(9)

Table 9. Oxygen interstitial positions and peak concentrations from Laue neutron diffraction of $P6_3/m$ $Nd_{(28+x)/3}Al_xSi_{6-x}O_{26}$ for x = 0.5, 1.0 and 1.5 at 100K, arranged from highest to lowest concentration.

	x	y	z	Conc. (Å^{-3})
x = 0.5				
$O_{Int}1$	0.6888	0.0324	0.1431	0.069
$O_{Int}2$	0.8069	0.0350	0.1261	0.065
$O_{Int}3$	0.9272	-0.0014	0.1058	0.064
$O_{Int}4$	0.7760	0.1509	1/4	0.064
$O_{Int}5$	0.8026	0.1129	1/4	0.064
$O_{Int}6$	0.4142	0.5105	1/4	0.062
$O_{Int}7$	0.7600	0.1197	0.1625	0.062
x = 1.0				
$O_{Int}1$	0.0700	0.2853	0.1405	0.065
$O_{Int}2$	0.3816	0.5552	0.1616	0.065
$O_{Int}3$	0.8045	0.0307	0.1096	0.060
$O_{Int}4$	0.5319	0.1348	0.0377	0.059
$O_{Int}5$	0.5545	0.1557	0.1357	0.059
x = 1.5				
$O_{Int}1$	0.4882	0.0371	1/4	0.055
$O_{Int}2$	0.6129	0.1592	1/4	0.053
$O_{Int}3$	0.4471	0.4636	1/4	0.053
$O_{Int}4$	0.5866	0.2295	1/4	0.053

Table 10. Refined atomic parameters from fixed wavelength neutron diffraction of as-grown and annealed $P6_3/m$ $Nd_{9.33}Si_6O_{26}$ at room temperature.

Crystal sample	As-grown	Annealed
GOF	6.51	5.96
R (%)	5.14	3.99
R_w (%)	7.57	7.20
Nd(1),4*f*,($^1/_3$ $^2/_3$ z)		
z	-0.0011(2)	-0.0011(2)
Occupancy	0.889(8)	0.844(7)
U_{iso} (Å^2)	0.0154(5)	0.0136(5)
Nd(2),6*h*,(*x y* $^1/_4$)		
x	0.0106(1)	0.0113(1)
y	0.2404(1)	0.2423(1)
U_{iso} (Å^2)	0.0093(4)	0.0071(4)
Si, 6*h*, (*x y* $^1/_4$)		
x	0.4009(2)	0.4003(2)
y	0.3719(2)	0.3711(2)
U_{iso} (Å^2)	0.0086(6)	0.0069(5)
O(1), 6*h*, (*x y* $^1/_4$)		
x	0.3228(2)	0.3213(2)
y	0.4872(2)	0.4856(2)
U_{iso} (Å^2)	0.0220(6)	0.0209(6)
O(2), 6*h*, (*x y* $^1/_4$)		
x	0.5967(2)	0.5956(2)
y	0.4735(2)	0.4734(2)
U_{iso} (Å^2)	0.0176(5)	0.0153(5)

O(3), 12*i*, (*x y z*)		
Occupancy	0.75(1)	0.72(1)
x	0.3528(5)	0.3536(5)
y	0.2550(2)	0.2545(2)
z	0.0620(3)	0.0612(3)
U_{iso} (Å^2)	0.0155(8)	0.0128(8)
O(3)', 12*i*, (*x y z*)		
Occupancy	0.25(1)	0.28(1)
x	0.304(1)	0.307(1)
y	0.2442(8)	0.2438(7)
z	0.086(1)	0.0846(9)
U_{iso} (Å^2)	0.0155(8)	0.0128(8)
O(4), 2*a*, (0 0 $^1/_4$)		
Occupancy	0.96(2)	1.04(1)
U_{iso} (Å^2)	0.031(1)	0.0225(8)

Table 11. Refined anisotropic atomic displacement parameters from fixed wavelength neutron diffraction of as-grown and annealed $P6_3/m$ $Nd_{9.33}Si_6O_{26}$ at room temperature.

Crystal sample	As-grown	Annealed
Nd (1), 4*f*, (1/3 2/3 z)		
U_{11}	0.0118(6)	0.0083(5)
U_{33}	0.0226(9)	0.0243(9)
Nd (2), 6*h*, (x y 1/4)		
U_{11}	0.0082(5)	0.0065(5)
U_{22}	0.0105(5)	0.0069(5)
U_{33}	0.0076(6)	0.0070(5)
U_{12}	0.0033(3)	0.0026(3)
Si/Al, 6*h*, (x y 1/4)		
U_{11}	0.0105(8)	0.0073(7)
U_{22}	0.0097(7)	0.0073(7)
U_{33}	0.0060(7)	0.0063(7)
U_{12}	0.0055(6)	0.0038(6)
O (1), 6*h*, (x y 1/4)		
U_{11}	0.0339(8)	0.0309(8)
U_{22}	0.0300(8)	0.0292(8)
U_{33}	0.0163(7)	0.0170(7)
U_{12}	0.0267(7)	0.0259(7)
O (2), 6*h*, (x y 1/4)		
U_{11}	0.0127(7)	0.0099(6)
U_{22}	0.0128(6)	0.0101(6)
U_{33}	0.0232(8)	0.0212(7)
U_{12}	0.0033(5)	0.0014(4)
O (3), 12*i*, (x y z)		
U_{11}	0.025(1)	0.020(2)
U_{22}	0.0165(6)	0.0132(6)
U_{33}	0.0084(8)	0.0072(8)
U_{12}	0.0130(8)	0.0095(8)
U_{13}	-0.0054(8)	-0.0034(8)
U_{23}	-0.0040(4)	-0.0030(4)
O (4), 2*a*, (0 0 1/4)		
U_{11}	0.015(1)	0.0138(9)
U_{33}	0.062(2)	0.040(2)

Table 12. Oxygen interstitial positions and peak concentrations from fixed wavelength neutron diffraction of as-grown and annealed $P6_3/m$ $Nd_{9.33}Si_6O_{26}$ at room temperature, arranged from highest to lowest concentration.

	x	y	z	Conc. (Å^{-3})
As-grown				
$O_{Int}1$	0.9844	0.0042	0.0618	0.10
$O_{Int}2$	0.1003	0.3392	0.0574	0.081
$O_{Int}3$	0.7409	0.0887	0.1930	0.074
$O_{Int}4$	0.6952	0.8210	1/4	0.064
$O_{Int}5$	0.5358	0.1373	0.1276	0.060
$O_{Int}6$	0.3958	0.5243	0.1206	0.060
Annealed				
$O_{Int}1$	0.7527	0.0505	1/4	0.055
$O_{Int}2$	0.8184	0.1413	1/4	0.050
$O_{Int}3$	0.0819	0.3374	0.0478	0.045
$O_{Int}4$	0.3858	0.5979	0.1666	0.040
$O_{Int}5$	0.5423	0.1386	0.0868	0.036
$O_{Int}6$	0.4169	0.5739	0.0634	0.036
$O_{Int}7$	0.1688	0.1724	1/4	0.033

Table 13. Raman shifts (cm^{-1}) of annealed $Nd_{9.33}Si_6O_{26}$ crystal derived from profile fitting of *zz*, *uz* and *uv* spectra, yielding A_g, E_{1g} and E_{2g} modes, respectively.

	A_g modes	E_{1g} modes	E_{2g} modes
	132.1	167.6	159.5
	168.7	187.2	190.5
	209.9	217.6	211.1
	230.7	233.2	232.7
	270.0	263.8	259.1
	291.7	295.0	292.6
	308.5	304.7	325.0
	326.9	348.6	361.6
	372.6	361.8	383.3
	391.8	391.5	401.0
	433.4 vb	413.7	431.6
	514.5 vb	438.7	448.8 b
	526.7	481.5	527.0
	547.1	527.8	555.7
	574.4 wb	533.1	579.9
	853.0	837.6	853.5
	862.8	855.1	862.4
	873.6	873.1	886.7 b
	903.0	902.1	935.3
	915.2	932.7	975.1
	938.2	976.0	990.2
	984.2	989.8	
Total:	**22**	**22**	**21**

REFERENCES

(1) Stambouli, A. B.; Traversa, E. *Renewable and Sustainable Energy Reviews* **2002**, *6*, 433.

(2) Minh, N. Q. *J. Am. Ceram. Soc.* **1993**, *76*, 563.

(3) Carrette, L.; Friedrich, K. A.; Stimming, U. *Fuel Cells* **2001**, *1*, 5.

(4) Ishihara, T.; Sammes, N. M.; Yamamoto, O. In *High Temperature Solid Oxide Fuel Cells: Fundamentals, Design and Applications*; Singhal, S., Kendall, K., Eds.; Elsevier: Oxford, 2003, p 83.

(5) Nakayama, S.; Sakamoto, M. *J. Eur. Ceram. Soc.* **1998**, *18*, 1413.

(6) Baikie, T.; Ng, M. H. G.; Madhavi, S.; Pramana, S. S.; Blake, K.; Elcombe, M.; White, T. J. *Dalton Trans.* **2009**, 6722.

(7) Pramana, S. S.; Klooster, W. T.; White, T. J. *J. Solid State Chem.* **2008**, *181*, 1717.

(8) Masubuchi, Y.; Higuchi, M.; Takeda, T.; Kikkawa, S. *Solid State Ionics* **2006**, *177*, 263.

(9) Tolchard, J. R.; Islam, M. S.; Slater, P. R. *J. Mater. Chem.* **2003**, *13*, 1956.

(10) Kendrick, E.; Islam, M. S.; Slater, P. R. *J. Mater. Chem.* **2007**, *17*, 3104.

(11) Abram, E. J.; Sinclair, D. C.; West, A. R. *J. Mater. Chem.* **2001**, *11*, 1978.

(12) Slater, P. R.; Sansom, J. E. H.; Tolchard, J. R. *Chem. Rec.* **2004**, *4*, 373.

(13) Arikawa, H.; Nishiguchi, H.; Ishihara, T.; Takita, Y. *Solid State Ionics* **2000**, *136-137*, 31.

(14) Pramana, S. S.; Klooster, W. T.; White, T. J. *Acta Crystallogr. B* **2007**, *63*, 597.

(15) Jones, A.; Slater, P. R.; Islam, M. S. *Chem. Mater.* **2008**, *20*, 5055.

(16) Béchade, E.; Masson, O.; Iwata, T.; Julien, I.; Fukuda, K.; Thomas, P.; Champion, E. *Chem. Mater.* **2009**, *21*, 2508.

(17) Matsunaga, K.; Toyoura, K. *J. Mater. Chem.* **2012**, *22*, 7265.

(18) Guillot, S.; Beaudet-Savignat, S.; Lambert, S.; Vannier, R.-N.; Roussel, P.; Porcher, F. *J. Solid State Chem.* **2009**, *182*, 3358.

(19) Fukuda, K.; Asaka, T.; Okino, M.; Berghout, A.; Béchade, E.; Masson, O.; Julien, I.; Thomas, P. *Solid State Ionics* **2012**, *217*, 40.

(20) Nakayama, S.; Higuchi, M. *J. Mater. Sci. Lett.* **2001**, *20*, 913.

(21) An, T.; Baikie, T.; Wei, F.; Li, H.; Brink, F.; Wei, J.; Ngoh, S. L.; White, T. J.; Kloc, C. *J. Cryst. Growth* **2011**, *333*, 70.

(22) An, T.; Baikie, T.; Wei, F.; Pramana, S. S.; Schreyer, M. K.; Piltz, R. O.; Shin, J. F.; Wei, J.; Slater, P. R.; White, T. J. *Chem. Mater.* **2013**, *25*, 1109.

(23) Okudera, H.; Yoshiasa, A.; Masubuchi, Y.; Higuchi, M.; Kikkawa, S. *Z. Kristallogr.* **2004**, *219*, 27.

(24) An, T.; Baikie, T.; Herrin, J.; Brink, F.; Shin, J. F.; Slater, P. R.; Li, S.; White, T. J. *J. Am. Ceram. Soc.* **2013**.

(25) An, T.; Orera, A.; Baikie, T.; Herrin, J. S.; Piltz, R. O.; Slater, P. R.; White, T. J.; Sanjuán, M. L. *Inorg. Chem.* **2014**, *53*, 9416.

(26) Campbell, J. W. *J. Appl. Crystallogr.* **1995**, *28*, 228.

(27) Campbell, J. W.; Hao, Q.; Harding, M. M.; Nguti, N. D.; Wilkinson, C. *J. Appl. Crystallogr.* **1998**, *31*, 496.

(28) Wilkinson, C.; Khamis, H. W.; Stansfield, R. F. D.; McIntyre, G. J. *J. Appl. Crystallogr.* **1988**, *21*, 471.

(29) Prince, E.; Wilkinson, C.; McIntyre, G. J. *J. Appl. Crystallogr.* **1997**, *30*, 133.

(30) Campbell, J. W.; Habash, J.; Helliwell, J. R.; Moffat, K. *Inform. Q. Protein Crystallogr.* **1986**, *18*, 23.

(31) Petricek, V.; Dusek, M.; Palatinus, L. Institute of Physics, Praha, Czech Republic, 2006.

(32) Momma, K.; Izumi, F. *J. Appl. Cryst.* **2008**, *41*, 653.

(33) Scherf, C.; Institut für Kristallographie ed.; RWTH Aachen: Aachen, Germany, 1998, p Program for data reduction of DIF4.

(34) McIntyre, G.; Institut Laue-Langevin: Grenoble, France, 1983, p Program for calculating absorption.

(35) Hutanu, V.; Meven, M.; Heger, G. *Physica B* **2007**, *397*, 135.

(36) Lambert, S.; Vincent, A.; Bruneton, E.; Beaudet-Savignat, S.; Guillet, F.; Minot, B.; Bouree, F. *J. Solid State Chem.* **2006**, *179*, 2602.

(37) Guillot, S.; Beaudet-Savignat, S.; Lambert, S.; Roussel, P.; Tricot, G.; Vannier, R.-N.; Rubbens, A. *J. Raman Spectrosc.* **2011**, *42*, 1455.

(38) Lucazeau, G.; Sergent, N.; Pagnier, T.; Shaula, A.; Kharton, V.; Marques, F. M. B. *J. Raman Spectrosc.* **2007**, *38*, 21.

(39) Orera, A.; Kendrick, E.; Apperley, D. C.; Orera, V. M.; Slater, P. R. *Dalton Trans.* **2008**, 5296.

(40) Smirnov, M.; Sukhomlinov, S.; Mirgorodsky, A.; Masson, O.; Béchade, E.; Colas, M.; Merle-Méjean, T.; Julien, I.; Thomas, P. *J. Raman Spectrosc.* **2010**, *41*, 1700.

(41) Wu, R.; Pan, W.; Ren, X.; Wan, C.; Qu, Z.; Du, A. *Acta Mater.* **2012**, *60*, 5536.

(42) Shannon, R. D. *Acta Crystallogr. Sect. A* **1976**, *32*, 751.

(43) Baikie, T.; Pramana, S. S.; Ferraris, C.; Huang, Y.; Kendrick, E.; Knight, Kevin S.; Ahmad, Z.; White, T. J. *Acta Crystallogr. Sect. B* **2010**, *66*, 1.

(44) Ali, R.; Yashima, M.; Matsushita, Y.; Yoshioka, H.; Ohoyama, K.; Izumi, F. *Chem. Mater.* **2008**, *20*, 5203.

(45) An, T.; Baikie, T.; Weyland, M.; Shin, J. F.; Slater, P. R.; Wei, J.; White, T. J. *Chem. Mater.* **2015**, *27*, 1217.

(46) Sansom, J. E. H.; Tolchard, J. R.; Islam, M. S.; Apperley, D.; Slater, P. R. *J. Mater. Chem.* **2006**, *16*, 1410.

TOC Graphic